Micropatterned silicone elastomer substrates for high resolution analysis of cellular force patterns

Claudia M. Cesa, Norbert Kirchgeßner, Dirk Mayer, Ulrich S. Schwarz, Bernd Hoffmann, and Rudolf Merkel

Citation: Review of Scientific Instruments **78**, 034301 (2007);
View online: https://doi.org/10.1063/1.2712870
View Table of Contents: http://aip.scitation.org/toc/rsi/78/3
Published by the American Institute of Physics

Articles you may be interested in

Oscillator clustering in a resource distribution chain
Chaos: An Interdisciplinary Journal of Nonlinear Science **15**, 013704 (2005); 10.1063/1.1852151

Theoretical determination of parity-violating vibrational frequency differences between the enantiomers of chiral molecules
The Journal of Chemical Physics **121**, 9959 (2004); 10.1063/1.1807815

Arnold tongues in human cardiorespiratory systems
Chaos: An Interdisciplinary Journal of Nonlinear Science **14**, 1 (2003); 10.1063/1.1620990

The effect of surface roughness on the adhesion of elastic plates with application to biological systems
The Journal of Chemical Physics **119**, 11437 (2003); 10.1063/1.1621854

On the mechanism of adhesion in biological systems
The Journal of Chemical Physics **118**, 7614 (2003); 10.1063/1.1562192

Effect of pulse polarity and energy on ultrasound-induced lung hemorrhage in adult rats
The Journal of the Acoustical Society of America **113**, 2912 (2003); 10.1121/1.1559176

Micropatterned silicone elastomer substrates for high resolution analysis of cellular force patterns

Claudia M. Cesa and Norbert Kirchgeßner
IBN-4, Biomechanics, Institute of Bio- and Nanosystems, Research Centre Jülich, 52425 Jülich, Germany

Dirk Mayer
IBN-2, Bioelectronics, Institute of Bio- and Nanosystems, Research Centre Jülich, 52425 Jülich, Germany

Ulrich S. Schwarz
Heidelberg University, Im Neuenheimer Feld 293, 69120 Heidelberg, Germany

Bernd Hoffmann and Rudolf Merkel[a)]
IBN-4, Biomechanics, Institute of Bio- and Nanosystems, Research Centre Jülich, 52425 Jülich, Germany

(Received 25 October 2006; accepted 29 January 2007; published online 19 March 2007)

Cellular forces are closely related to many physiological processes, including cell migration, growth, division, and differentiation. Here, we describe newly developed techniques to measure these forces with high spatial resolution. Our approach is based on ultrasoft silicone elastomer films with a regular microstructure molded into the surface. Mechanical forces applied by living cells to such films result in elastomer deformation which can be quantified by video microscopy and digital image processing. From this deformation field forces can be calculated. Here we give detailed accounts of the following issues: (1) the preparation of silicon wafers as molds for the microstructures, (2) the fabrication of microstructured elastomer substrates, (3) the in-depth characterization of the mechanical properties of these elastomers, (4) the image processing algorithms for the extraction of cellular deformation fields, and (5) the generalized first moment tensor as a robust mathematical tool to characterize whole cell activity. We present prototype experiments on living myocytes as well as on cardiac fibroblasts and discuss the characteristics and performance of our force measurement technique. © *2007 American Institute of Physics.*
[DOI: 10.1063/1.2712870]

I. INTRODUCTION

For most animal cell types adhesion to extracellular matrices or to other cells is an essential prerequisite for survival, migration, growth, division, and differentiation. A rapidly increasing number of research results accumulated over the last decade demonstrate that in addition to biochemical signals, mechanical forces acting at the interface between cells and their environment are key regulators of these physiological processes.[1–4] One prominent example is the differentiation of fibroblasts to myofibroblasts. Here, cells recognize substrate elasticities via mechanosensing processes resulting in morphological and functional modifications.[5] The molecules mediating cell adhesion form well defined aggregates within the cell-substrate contact area which are believed to act both as force transmission and signaling centers. The best known examples are focal adhesions, large integrin-based cell-matrix contacts which form on flat and rigid substrates. Obviously, measurement techniques sensitive enough to determine the forces at the level of single contacts are mandatory to elucidate the role of focal adhesion sites in cell force transmission and sensing.

A first breakthrough towards such techniques was the wrinkling assay of Harris.[6] In this assay cells are cultivated on a thin elastic lamella which forms folds due to cell forces. However, quantitative evaluation of the observed patterns is very difficult because wrinkling is a highly nonlinear process. Later on, wrinkling was effectively suppressed by using very soft elastic layers bonded to microscope coverslips.[7–10]

In this approach cell forces act on the top surface of the elastic layer which is free to move. These forces result in a mechanical deformation of the layer which is entirely determined by the distribution of forces, the elastic properties of the film, and the boundary conditions. Thus, after suitable calibration, the distribution of forces can be inferred from the measurable displacement of the film surface. In the simplest approximation, one can approximate the elastic film by an elastic half space for which the mathematical solutions of the mechanical problem are well established.

In such experiments the displacement field at the elastic surface is determined directly (Fig. 1). Mathematically, this deformation field is derived from the force field acting on the surface by a convolution with Green's tensor. Thus, calculating cellular force distributions from traction force microscopy amounts to unfolding the measured displacement field of the substrate with appropriate Green's tensor.[11] This is a numerically ill-posed problem whose approximate solutions can be obtained by regularization and nonlinear data fitting.[12,13] At present, the basic ideas of traction force mi-

[a)]Author to whom correspondence should be addressed; FAX: ++49 (0)2461 61 3907; electronic mail: r.merkel@fz-juelich.de

 © 2007 American Institute of Physics

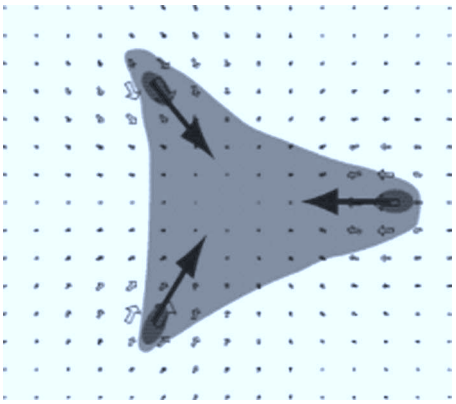

FIG. 1. The basic principle of traction force microscopy: A cell (gray, triangular) adheres to an elastic substrate predominantly at specific locations (gray ellipses). Mechanical forces (full arrows) result in a deformation of the substrate (open arrows) which decays with increasing distance from the sites of force application.

croscopy are well documented.[7–10,14,15] However, preparing microstructured, ultrasoft substrates for cell force microscopy, characterizing them, and establishing the necessary image processing algorithms still present major challenges. In this article, we describe how progress in these aspects can be achieved.

In general, ultrasoft substrates for cell force measurement are prepared from weakly cross-linked polymers. Most researchers working with cells on soft elastic substrates use the hydrogel polyacrylamide because its stiffness can be easily tuned over a large range from few hundred pascals to megapascals. Moreover, due to its widespread use for gel electrophoresis most biochemists are very experienced in handling and preparing this material. However, there are several disadvantages connected to this choice. The monomers used are toxic and surface biofunctionalization is tedious. Moreover, topographic surface microstructures in polyacrylamide are for all practical purposes invisible in the light microscope because of the very similar optical properties of polyacrylamide and water. Therefore, marker beads have to be embedded in order to evaluate deformations. However, it is hardly possible to achieve homogeneous distributions of beads. For this reason, stationary cells (most cells) are very difficult to analyze because resting positions of beads (i.e., the reference state without force) are unknown. In addition, upon deformation, water flows in the gel, possibly changing its microstructure. In our work, we chose polydimethylsiloxane (PDMS) as an alternative material system for measuring cellular forces.[5,10] PDMS is biocompatible and does not take up water. Thus cross-linked PDMS can be stored and characterized in ambient air. Surface functionalization is easy because proteins attach to the hydrophobic surface by physisorption. In addition, no flow of solvent occurs within the material upon force application. As evidenced by its widespread use in microcontact printing,[16] PDMS is especially suited for micropatterning, which in our context can be used to track deformations caused by cellular traction. To this end we used silicon wafers with regular surface patterns as molds to cross-link PDMS films on top. The resulting elastomer films bear the imprint of the mold as topographic surface pattern.

One disadvantage of traction force microscopy on continuous soft elastic substrates is that calculations based on elasticity theory have to be employed in order to calculate the cellular forces from the deformation pattern. In principle, a more straightforward force analysis is possible by cultivating cells on top of arrays of soft PDMS pillars.[17,18] However, here the simplicity of force measurement comes at the expense of very peculiar conditions for the cells whose adhesion areas are split into several isolated parts on top of a very marked topography.

The main purpose of this publication is a careful analysis of the properties of microstructured PDMS elastomer films as specific type of ultrasoft substrates for cell force microscopy and a description of the methods used to prepare them. We show that these extensively characterized flat substrates are well suited for accurate force analysis at single focal adhesions. Moreover we introduced a generalized first moment (GFM) to quantify the overall mechanical contraction of cells. This moment is stable to number and location of focal adhesion sites used for calculation and thus a reliable tool for the comparison of different cells or cell types.

II. EXPERIMENTAL SETUP AND PROCEDURE

A. Preparation of hard molds for micropatterning

Standard lithographic techniques from semiconductor technology[19] were used to prepare hard molds for micropatterning elastomers. We preferred silicon dioxide structures to photoresist structures because of their toughness to mechanical forces exerted in subsequent steps.

Silicon wafers (3 in. diameter, ⟨100⟩ crystallographic orientation, Silicon Materials, Landsberg, Germany) were wet oxidized at 1100 °C resulting in a layer of SiO_2 of controlled thickness. Oxidized wafers were coated with a layer of positive photoresist (AZ 5214E diluted 2:1 with AZ 1500 thinner, Microchemicals GmbH, Ulm, Germany). Contact photolithography at 365 nm was used. The lithography mask consisted of a square lattice (with a lattice constant of 3.5 μm) of chromium features (2.5 μm diameter) on bare quartz. Subsequently, developing in MIF326 (Microchemicals) removed the resist in the exposed areas and resulted in an array of microdots exhibiting a height similar to the one of the photoresist film (~500 nm).

Transfer of the structure to the SiO_2 layer was performed in two successive steps of reactive ion etching. First, uncovered silicon dioxide was removed by dry etching with CHF_3/CF_4 (1:1 ratio). Subsequently, the remaining resist was converted into ash by oxygen plasma. The height of the final structures was adjusted by varying the thickness of the oxide layer.

B. Preparation of micropatterned elastomeric surfaces

Elastomer substrates were prepared from PDMS using replica molding.[16] We used a premixed PDMS system (Sylgard 184, Dow Corning, Midland, MI) containing a vinyl

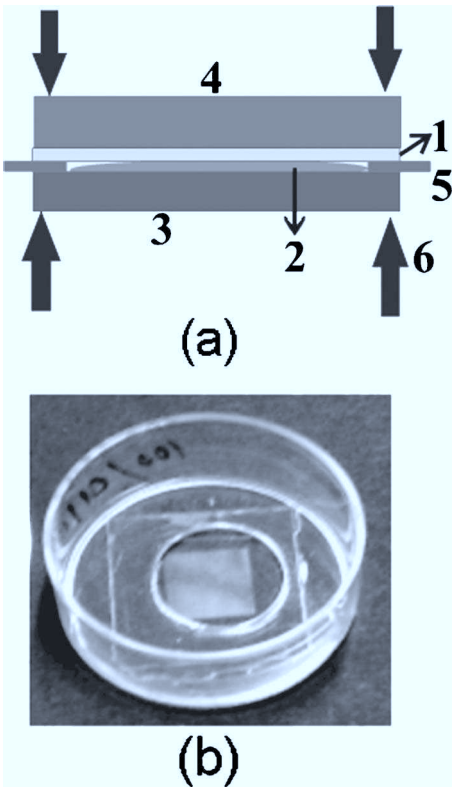

FIG. 2. Preparation of microstructured elastomeric surfaces: (a) A drop of prepolymer mixture (2) was dispensed on the silanized SiO_2 mold (3); a coverslip (1) was placed on top. To control the thickness of the film, glass spacers (5) were used. Uniform spreading of the mixture on the mold was ensured by fixation (6) of the sandwich with metal clamps between a piece of glass microslide (4) and the SiO_2 mold (3). After cross-linking of the elastomer the mold was removed, resulting in a uniform, microstructured elastomer film on top of a coverslip. Such elastomeric surfaces were glued to the undersides of perforated Petri dishes (b).

terminated polydimethylsiloxane as base and a methylhydrosiloxane-dimethylsiloxane copolymer as curing agent (cross-linker). The prepolymer mixture (base to curing agent ratios ranging between 35:1 and 55:1) was poured over a silanized $(1H,1H',2H,2H'$-perfluorooctyl-trichlorosilane, Sigma, St. Louis, MO) silicon dioxide mold (see above). Silanization was performed at room temperature by exposing the samples for 15–30 min to the silane vapor in vacuum. Subsequently, a thin microscopy coverslip (80 μm, Menzel GmbH, Braunschweig, Germany) was placed on the PDMS layer coating the silicon mold [Fig. 2(a)]. Uniform PDMS layer thickness was achieved using 100 μm thick glass spacers (cut from coverslips) between the coverslip and the mold. A fittingly cut piece of glass microslide was placed on top of the coverslip. The whole sandwich was then compressed by clamping with two paper clips at the spacer supported edges [Fig. 2(a)]. Subsequently, cross-linking of the elastomer was performed at 60 °C overnight. After PDMS cross-linking, the elastomer was released from the mold. This resulted in a thin, uniform layer of elastomer, fixed on top of a glass coverslip exhibiting a three dimensional microstructure on its surface. By using thin coverslips the overall thickness of the system was about 180 μm and therefore optimized for the use of high power microscope lenses which are optically corrected for a coverslip thickness of 170 μm. The final substrates were glued to the undersides of Petri dishes with 2 cm holes drilled through the bottoms [Fig. 2(b)].

Thickness, uniformity, and reproducibility of elastomer substrates were checked using a confocal microscope (LSM 510, Zeiss, Jena, Germany) equipped with an Epiplan 50 $\times$0.70 lens. Thickness variations within the micropatterned areas did not exceed 5% independent of the mixing ratio used.

The depth of the PDMS micropattern was examined using atomic force microscopy (DI MultiMode, Veeco). Samples were analyzed in air, using silicon cantilevers of a mean resonance frequency of 270 kHz and tapping mode.

C. Preparation of the calibration samples

A detailed knowledge of the mechanical material parameters of the elastomer films is mandatory for the calculation of cell forces. Due to the extreme adhesiveness of soft PDMS we had to develop our own methods for material characterization. In essence, we prepared test pieces of convenient size in dissolvable molds. This circumvented the problems of working with tiny and very sticky samples.

Cylindrical test pieces were prepared using channels in agarose. A metal cylinder (10 cm length) was placed vertically on a Teflon plate and filled with a 2% solution of molten agarose (Sigma) to a height of 1 cm. After agarose gelation, glass capillaries with a diameter of 1.4 mm were stuck vertically into the agarose layer. Subsequently, the metal cylinder was filled to the top with molten agarose.

After agarose hardening, the glass capillaries were removed. To prevent sample defects residual water in the channels was dried out by argon flushing. The dry channels were carefully filled with premixed, yet still uncross-linked PDMS using a syringe. The whole assembly was covered with parafilm to prevent agarose drying and baked at 60 °C overnight. Cross-linked PDMS cylinders were either blown out of the agarose mold with a syringe or removed by melting the agarose block in boiling water. Later, PDMS cylinders were washed three times in boiling water to remove residual agarose.

For calibration experiments, samples were mounted vertically between a precision scale (AB204-S, Mettler-Toledo, Greifensee, Switzerland) and a micromanipulator (MHW-3, Narishige International, Tokyo, Japan). Accurate alignment of the samples was imperative to prevent shear forces and to minimize focus changes upon stretching. Samples were observed using a stereo-microscope (Stemi 2000, Zeiss) connected to a charge-coupled device (CCD) camera (XCD-X710, Sony, Tokyo, Japan). Scale readings, i.e., the acting forces, were automatically recorded every 0.25 s. Elastomer rods were stretched in five successive steps, each resulting in a relative elongation of approximately 1%, followed by a subsequent equilibration period of 30–50 min. CCD images were captured using IC CAPTURE 2.0 (The Imaging Source, Charlotte, NC) software. All stretching steps and the complete, stepwise release of the samples were recorded. Deformations were measured at the middle of the samples to avoid errors due to possible waist formation. As markers for sample deformation, chalk dust was applied to the surface of the rods. The focus was set to the edges of the sample, at the

median plane, in order to allow accurate measurement of the sample diameter. Evaluation of the measurements was performed using routines developed with MATLAB (Release 14, Natick, MA).

D. Isolation and culture of cells

Cardiac fibroblasts as well as myocytes were isolated from 19 day old Wistar rat embryos. In brief, CO_2 anesthetized pregnant rats were decapitated, and the embryos were removed and decapitated under sterile conditions. The heart of each embryo was quickly isolated, washed in Hank's balanced salt solution (HBSS, Sigma), cut into small pieces, and digested in a 0.5% Trypsin/0.2% EDTA solution in HBSS to disintegrate the tissue. The resulting cell suspension was further incubated with 100 μl DNase solution (10.000 u/ml Sigma). Cells were collected by centrifugation at 200 g. Cells were seeded on PDMS surfaces which were coated with 2.5 $\mu g/cm^2$ human plasma fibronectin (BD Biosciences, San Jose, CA). After 30 min nonadherent cells (primarily myocytes as they adhere slower than cardiac fibroblasts) were taken away with the supernatant and plated on fresh fibronectin coated PDMS surfaces. Cells were maintained in F10 Ham's medium supplemented with 10% fetal bovine serum, a 1:100 dilution of an antibiotic solution (10 000 units penicillin and 10 mg/ml streptomycin in 0.9% NaCl, Sigma), and a 1:200 dilution of solution containing insulin (1 mg/ml), transferrin (0.55 mg/ml), and sodium selenite (0.5 μg/ml) (Sigma) at 37 °C and 5% CO_2 in a humidified incubator.

E. Light microscopy techniques

Deformation fields were examined by reflection interference contrast microscopy (RICM) on an inverted light microscope (Axiovert 200, Zeiss) using a Plan-Neofluar 63 $\times$1.25 oil Ph3 antiflex lens (Zeiss). This technique allowed the visualization of both the micropattern under the cell and the focal adhesion sites by slightly changing the focus and adjusting the intensity of the light source. Image acquisition was performed using an ORCA ER CCD camera (Hamamatsu Photonics, Hamamatsu, Japan) and OPEN BOX as software (version 1.77, Informationssysteme Schilling, Munich, Germany). For control experiments, cell transfection was performed using Transit TM (Mirus BioCorporation, Madison, WI) as transfection reagent with a GFP-vinculin construct.[20]

III. EXPERIMENTAL RESULTS

A. Elastomer calibration

Reliable cell force analysis depends crucially on a quantitative understanding of the mechanical material properties of the soft substrate. Therefore, we developed a method to determine the mechanical parameters of PDMS elastomers. Small constant strains, in a similar range to those applied by adhered living cells, were applied to cylindrical samples made of PDMS elastomer. Identical base to curing agent ratios as used for cell substrates was taken. Cylindrical samples were chosen because their axial symmetry greatly facilitates strain measurement.

The calibration experiments on PDMS elastomer cylinders consisted in measuring the stress relaxation curve at constant strain. The deformation (i.e., axial and radial strains) of the sample was analyzed by tracking small chalk particles applied previously to the very sticky elastomer surface.

Radial strain was measured by splitting the observation area vertically in two halves. The mean horizontal positions of all particles in each sector were determined for all images. As the distance of these "centers of gravity" is directly proportional to the diameter of the rod, this procedure yields the radial strain directly. For the axial strain the observation area was split horizontally and the vertical coordinates were averaged. Axial strains were below 5%. The features on the sample were localized by taking maxima of the local variance. Tracking them in subsequent images of the sequence was done by normalized cross correlation.[21] All tracked features contributed equally to the averaging, i.e., no weight factors were used.

For calculation of the diameters of PDMS cylinders images were taken and compared to an image of a glass capillary of known size. The outer borders of PDMS rods and glass capillaries were localized by finding the maxima of the local variance of the images. The sample diameter was measured in the first image of the elongation sequence where the sample was considered to be in the relaxed state although already under some slight stress to prevent bending under its own weight. Such prestress was of no importance as identical results were found using elongations of 50% and more (data not shown). For the relaxation sequence the last image of the sequence was used as reference for measuring the diameter when the sample came back to the starting position.

The material showed some viscoelastic behavior, i.e., force relaxation. As no changes in length or diameter of the cylinders occurred during relaxation it took place at constant strain [Fig. 3(a)]. This behavior is described by a stress relaxation function, $G(t)$, which is defined by $G(t)=\sigma(t)/\varepsilon$, where σ, denotes axial stress (i.e., tensile force per cross section area) and ε represents the constant axial strain. Figure 3 represents a force relaxation curve which is directly proportional to the stress relaxation curve. In all experiments the elastomer behaved essentially as an elastic solid, i.e., it withstood permanent forces without flowing. Moreover, the material response was linear, that is directly proportional to the applied stress. We approximated its viscoelastic response by $G(t)=E_\infty+E_1e^{-t/\tau}$, where E_∞ denotes the long time limit of the relaxation function, (E_1+E_∞) the short time limit, and τ the longest relaxation time of the material. The relaxing fraction of the response was always below 30% with relaxation times τ on the order of 20 min. In view of the low amount of relaxation we assumed standard Hookean material response in our cell force calculations. As Young's moduli we took G_∞ determined from the last 20 video frames of each relaxation period, i.e., E was determined about 30 min after stretching.

Poisson's ratio of a material is the ratio between relative transverse shrinkage and relative longitudinal extension upon uniaxial loading. The measurements yielded values close to 0.5 for every mixing ratio tested (Table I). Therefore, Poisson's ratio was approximated to 0.5 for subsequent cell force

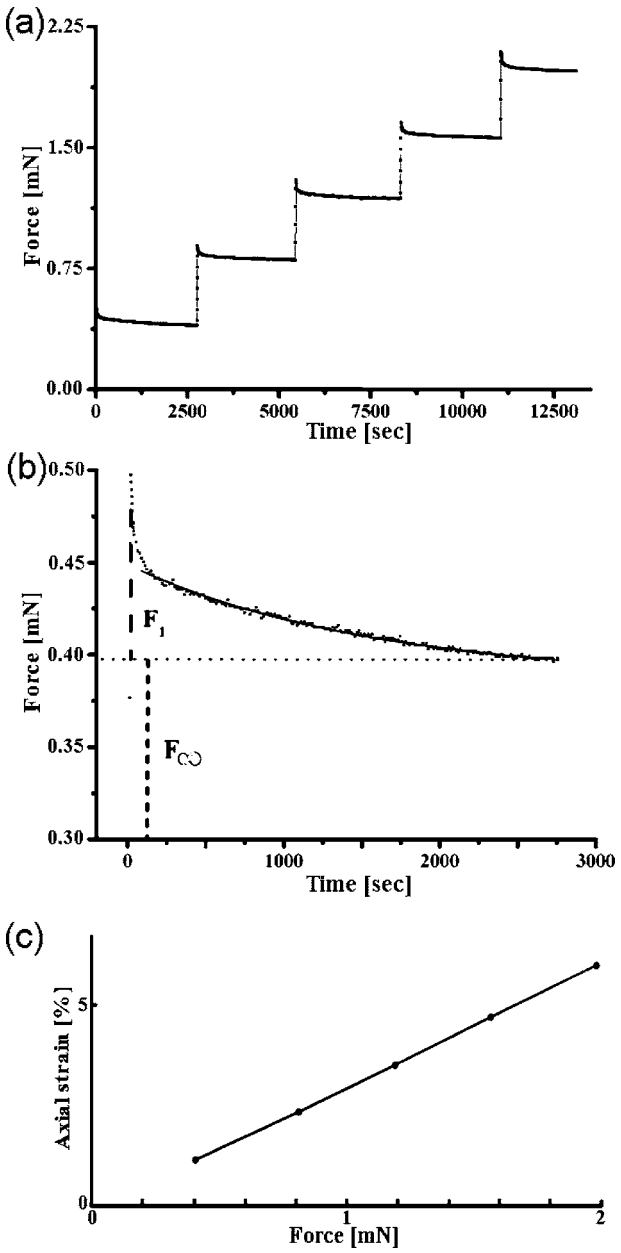

FIG. 3. Results of calibration experiments: (a) A PDMS cylinder (55:1 base to cross-linker ratio) was stretched in five successive steps. The resulting force relaxation curve is given. Sample diameter of 1.5 mm. (b) A single exponential fit to the relaxation function. Fit results: F_∞=0.39 mN; F_1 =0.06 mN; τ=1600 s. (c) The relative elongation of the sample varies linearly with the stress applied. In this example Young's modulus was 16 kN/m^2.

analyses. For each mixing ratio used Young's modulus as well as Poisson's ratio were analyzed on independent samples and found to be reproducible within 10% for both.

In addition to the bulk measurements we explored possible material inhomogeneity by observing the deformation field caused by a point force. To this end a syringe needle mounted in a micromanipulator was used to deform the film. The resulting deformation fields could be well fitted by the pattern expected for one point force. Local variations as expected in the presence of significant spatial variations in Young's modulus were not observed (data not shown).

These characterized elastomers were used for the preparation of micropatterned surfaces. For cell force analysis the micropattern needed to be deep enough to yield sufficient contrast in phase contrast and RICM microscopy but shallow enough to be ignored by the cell. Cellular pattern recognition would strongly interfere with cell behavior and morphology. Thus it had to be avoided. We found that different feature heights of the molds were optimum for the different mixing ratios of the elastomer used (100 nm at a mixing ratio of 35:1, 500 nm at 55:1). Moreover, we noticed a different pattern contrast in light microscopy depending on the mixing ratio used. The softer the elastomer was, the less contrast showed the features decorating its surface. Thus molding fidelity appeared to depend on elastomer stiffness. To test this, we analyzed two samples of extreme compositions, prepared with well characterized molds, using the atomic force microscopy (AFM) (Fig. 4). For a stiff elastomer surface (prepared in a 10:1 base to curing agent ratio and not further analyzed for Young's modulus and Poisson's ratio) molding resulted in a perfect reproduction of mold topography with relatively sharp edges and matching depth (approximately 500 nm) [Figs. 4(a) and 4(b)]. In contrast, for the softer elastomer (prepared in a 50:1 base to curing agent ratio, Young's modulus of 25 kN/m^2) the depths of the microstructures were with 50 nm much below the height of the mold used. Moreover, the imprint of the structure was very smooth with blurred features [Figs. 4(c) and 4(d)]. The microstructure as used for cell studies is very shallow (50 nm depth versus 100 μm film thickness). For this reason microdimples do not influence the elastic response of the layer.

While molding fidelity of individual dimples varied with elastomer stiffness, the regular grid was always faithfully reproduced. Over a field of view (130×100 μm^2), the individual points were found within 35 nm (standard deviation) from the expected position of the ideal grid. Thus the grid could serve as reference frame for the calculation of displacements.

TABLE I. Elastic parameters of the material. Values of Young's modulus (E) and Poisson's ratio (ν) for the five elastomer stiffnesses analyzed. The fourth column of the table gives the elastic fraction, averaged for the five different elongation steps of all samples analyzed. In the case of the release steps, the elastic fraction was even higher (data not shown).

Sylgard ratio base to curing agent	Young modulus (E) (kPa)	Poisson ratio (ν)	$\frac{E_\infty}{E_1+E_\infty}$ (%)
35:1	130±9	0.5	87
40:1	80±14	0.46	70
45:1	38±4	0.49	90
50:1	25±2	0.54	66
55:1	15±1	0.56	77

B. Determination of the displacement vector field (DVF)

As we used a regular lattice of microstructures we were able to extract the displacement vector field from single images. To this end, we fitted a regular grid to the data first and determined the displacements of the individual structures from the ideal grid later. The first step of the displacement

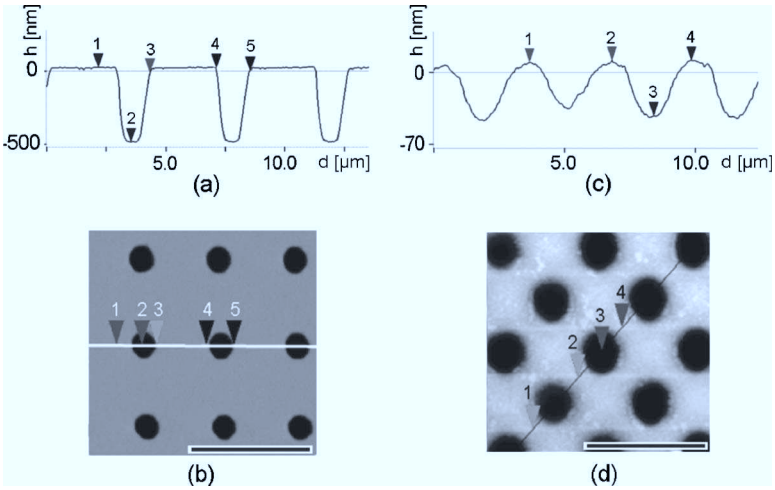

FIG. 4. AFM analysis of microstructures: Two microstructured PDMS surfaces were prepared in 10:1 [(a) and (b)] and 50:1 [(c) and (d)] ratios, respectively. Both surfaces were analyzed by AFM in air using tapping mode. Height profiles along the respective lines are given in (a) and (c). Numbers indicate identical positions. Note the different height scales in (a) and (c). Scale bars=5 μm.

determination was the localization of the grid points. For this purpose one point of the grid was interactively marked with a rectangle. On this region of interest we tested three synthetic point templates by normalized cross correlation at all possible positions. These templates were a paraboloid, a round dot with smoothed edges, and the same dot with a hole inside. They were all varied in size. The template with the highest normalized correlation coefficient[21] C was used for calculation of the correlation coefficients of the whole image. Local maxima of C exceeding an interactively chosen threshold (typically 0.7) were considered as grid points.

As we used a regular lattice we knew that the position $\mathbf{r}_{cl}$ of every point in the undeformed state of the grid was given by $\mathbf{r}_{cl}=\mathbf{g}_b+c\mathbf{g}_c+l\mathbf{g}_l$, where $\mathbf{g}_b$ is the base point of the grid and $\mathbf{g}_c$, $\mathbf{g}_l$ the grid vectors in column and line directions, respectively. The numbers of column c and line l of the point in the grid were integers and are called grid indices in the following.

In order to determine the displacement for each grid point we subtracted its position $\mathbf{r}_{cl}$ in the undeformed grid from its measured position $\mathbf{r}_m$. Therefore, we needed its grid indices (c,l) and the characteristic vectors of the grid $\mathbf{g}_b$, $\mathbf{g}_c$, and $\mathbf{g}_l$. The algorithm to determine the grid indices worked line by line. Its input values were the points of the deformed grid. These points were the result of the previous point search together with three interactively chosen points $\mathbf{p}_1$, $\mathbf{p}_2$, and $\mathbf{p}_3$ which span and defined the axes of the grid (first and last points of first column $P_c=[\mathbf{p}_1,\mathbf{p}_2]$ and first line $P_l=[\mathbf{p}_1,\mathbf{p}_3]$, respectively). Subsequently, the grid points of the marked grid column were processed as described in the next paragraph using P_c. This gave the grid position of the points of the first column and the grid vector in column direction $\mathbf{g}_c$. The same procedure was repeated with the marked grid line taking P_l and yielded the grid indices of the first line of the grid. Repetitive displacement of P_l by $\mathbf{g}_c$ and equal processing yielded the grid indices for the next grid lines, successively.

To find the grid indices of a line of points the Euclidean distance map[22] (EDM) was calculated from the points of the grid. It had the same size as the original image and contained the distance to the next found point in each pixel. The following procedure was applied to each line of the grid. The end points of the processed grid line were given as described above. A line between these two points was sampled on the EDM. This gave a vector that contained the distance to the next point. It looked like a triangular signal with minimal values at the positions of the found points. These distance values were used for a Fourier analysis which yielded the frequency f_l and grid constant of the current grid line. The location of adequate points was given by adding integer multiples of this grid constant to the first point of the line and gave the point positions of an undeformed grid. In order to neglect similar background structures that were located in between we considered only points which were closer than 20% of the grid constant to these positions. Thus, we identified most of the points belonging to the analyzed grid line. Their grid positions were the rounded values of the ratio of their position and the grid constant. Performing this operation for each grid line yielded a first estimation of the grid index for about 50% of all points found.

We calculated $\mathbf{g}_b$, $\mathbf{g}_c$, and $\mathbf{g}_l$ by an ordinary least squares fit using all measured positions $\mathbf{r}_{cl}$ and their grid indices to the equation above. Falsely allocated grid indices were eliminated by application of robust statistics. The vectors $\mathbf{g}_b$, $\mathbf{g}_c$, and $\mathbf{g}_l$ were now used to complete the grid on the whole image calculating all lattice positions at which no point was yet found. Local maxima of the normalized correlation coefficient C in the vicinity of these locations were inserted in the grid. Then the fitting procedure was repeated, resulting in the parameters of the undeformed grid in this image. These allowed us to calculate the point displacements from a regular square lattice in a single frame. The displacements of the grid points were found by taking a region of interest around each grid point in the first image of the sequence as template and tracking it through the image sequence by normalized cross correlation.

C. Mechanical force analysis of living cells at sites of single focal adhesions

Most mammalian cells adhere to surfaces and apply mechanical forces via focal adhesion sites or similar structures. The micropatterned elastomer substrates as calibrated above allowed us to analyze these forces in detail. For prototype

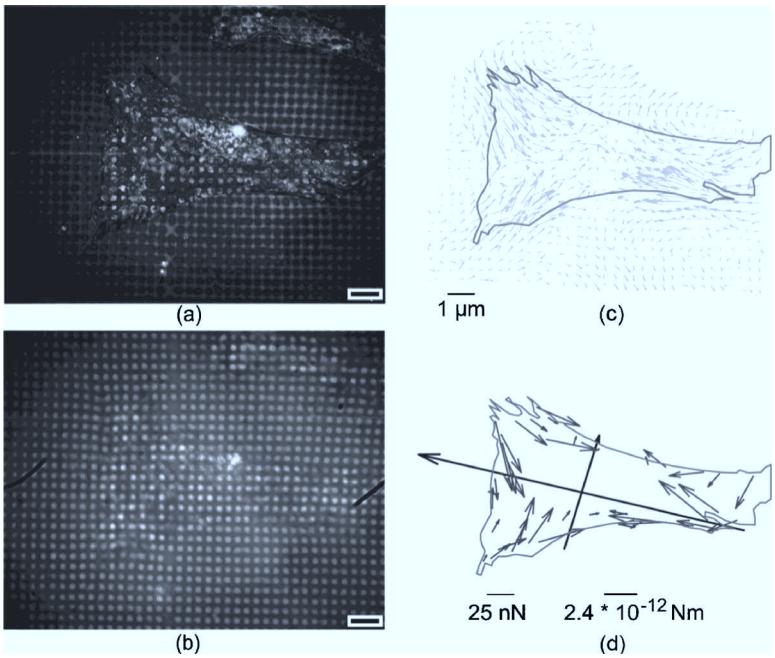

FIG. 5. Cell force analysis on myofibroblasts: To measure mechanical forces myofibroblasts were grown on 55:1 PDMS micropatterend surfaces. Adhesion sites (a) as well as the micropattern (b) were localized by RICM in single images. Subsequent image processing defined the displacement field (c) (gray arrows) from which cell forces applied at single adhesions were calculated (d) (black arrows). Bold arrows point in the direction of the eigenvectors of the generalized first moment tensor; their lengths are scaled by the corresponding eigenvalues (d). Scale bars=10 μm. Sum of contractile forces 940 nN.

experiments two different cell types with quite different mechanical behavior were chosen. The first cell types analyzed were myofibroblasts. These cells are responsible for constant contractions of tissues and organs, e.g., of the heart. They exhibit large focal adhesion sites and apply strong, permanent forces. The second cell type were myocytes displaying periodic and rapid contraction. Both cell types were isolated from embryonal rat heart and plated on elastic surfaces with Young's modulus of 16 kPa (55:1 ratio). Both cell types were morphologically unaffected by growth on elastic surfaces compared to growth on glass surfaces. After two days of incubation cells were analyzed by light microscopy using phase contrast and RICM techniques. RICM allowed the visualization of the micropattern even under the cells [Figs. 5(b) and 6(b)] and simultaneously the localization of focal adhesion sites [Figs. 5(a) and 6(a)]. As control, focal adhesion sites were additionally localized in fibroblasts by the GFP technology. For this purpose fibroblasts were transfected with GFP-vinculin, a well established marker for the identification of focal adhesions by fluorescence microscopy. Adhesions are seen as bright stripelike or triangular spots often in the periphery of the cell. It turned out that GFP-

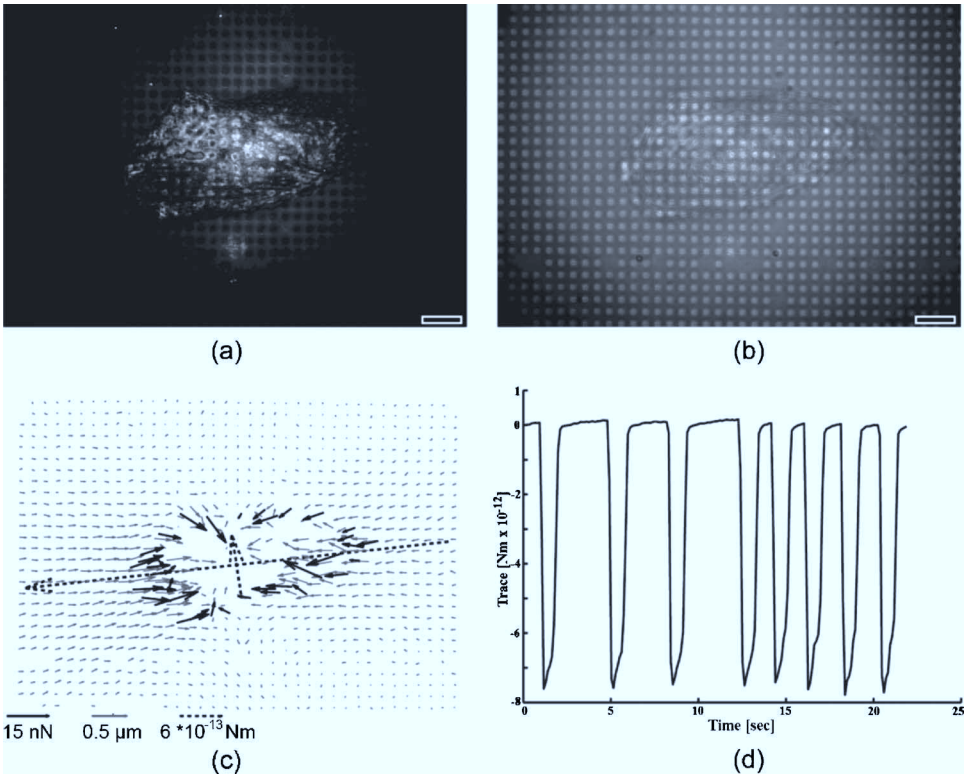

FIG. 6. Cell force analysis on cardiac myocytes: Cardiac myocytes on 55:1 PDMS surfaces. RICM images of a single adherent myocyte are shown in order to detect focal adhesion sites (a) as well as the micropattern (b). Given are single images of time lapse movies covering several cell contractions. (c) gives the deformation map (gray arrows) caused by forces at single focal adhesions (black arrows), as well as the eigenvectors of the generalized first moment (dotted back arrows). The sum of the eigenvalues (trace) of the generalized first moment tensor is plotted during periodic contractions of the cell (d). Note that the sum of the eigenvalues is essentially identical for each contraction. The peak values correspond to sums of contractile forces of approximately 300 nN. Scale bars =10 μm.

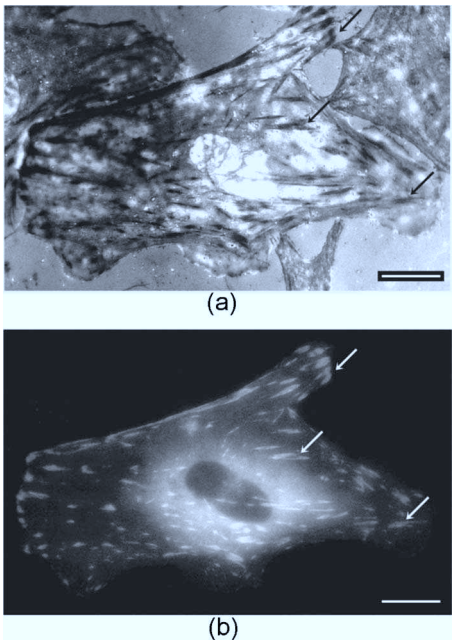

FIG. 7. RICM vs fluorescence: Freshly isolated myofibroblasts were seeded on a glass surface and subsequently transfected with GFP-vinculin. At day two after transfection cells were analyzed by RICM (a) and fluorescence (b). The sites of focal adhesions [bright areas in (b)] corresponded closely to dark areas in RICM. Some examples are marked by arrows. Scale bars $=10\ \mu$m.

vinculin signals corresponded to almost 100% to dark areas characterizing focal adhesion sites in RICM [Figs. 7(a) and 7(b)].[23,24]

Because fibroblasts are stationary cells, displacement fields as well as adhesion structures were localized on single images for these cells. The characterization of the deformation field varied for contracting myocytes, where image sequences spanning several contractions were used. For myofibroblasts, an ideal dot grid was fitted to the position of grid points displaced by the cell. The dot positions were measured by cross correlation with a synthetic template (see above). The displacements of the points from the expected grid were calculated and used for further cell force analyses [Figs. 5(c) and 6(c)]. In order to characterize forces applied upon myocyte contraction, grid points were localized first in the relaxed state, i.e., between two contractions. The image corresponding to the most relaxed phase of the cell was chosen as reference for the measurement of the deformation under cell traction. As this procedure compensates for the influence of minor grid inhomogeneity, displacement measurement was even more robust for myocytes than for fibroblasts. At each position of a grid point a region of interest was taken as template from the first image of the sequence. Such a point was tracked in subsequent images via normalized cross correlation. Focal adhesion sites were marked by hand for myocytes in the relaxed state.

Knowing the deformation fields and the origins of force application, forces were calculated by solving the inverse problem of elasticity[13,25] [Figs. 5(c), 6(c), and 6(d)]. In our algorithm the size of the focal adhesion sites was not considered. Instead, focal adhesions were approximated as point-like force application sites. For myocytes, forces per focal adhesion site in the range of 15 nN could be observed upon contraction. For myofibroblasts forces in the range of up to 60 nN could be detected for single adhesion sites. Contraction force patterns of myocytes were stable for the time analyzed [Fig. 6(d)]. Forces constantly applied at single focal adhesions of fibroblasts were also stable over the whole time period of cell analysis (2 h) (data not shown).

D. Characterization of whole cell contractions by a generalized first moment

Force analyses for every single adhesion site of a cell are very useful for determining when and where forces are applied by cells. However, in many instances one additionally needs to quantify the mechanical activity of a whole cell. This is necessary, for example, for the comparison of different cells or for cells exhibiting many adhesion sites in close proximity whose force distribution cannot be separated properly by a fitting algorithm.

Living cells are either stationary or move very slowly. Thus viscous forces in the external medium are negligible. Therefore the overall force and torque of the cell vanish. As most simple nonvanishing characteristic of the force distribution we used the generalized first moment $\overrightarrow{\overrightarrow{M}}$ (also called force dipolar tensor). For point forces $\mathbf{f}(i)$ applied at positions $\mathbf{r}(i)$, it was defined as follows:

$$\overrightarrow{\overrightarrow{M}} = \sum_i \begin{pmatrix} x(i)\cdot f_x(i) & y(i)\cdot f_x(i) \\ x(i)\cdot f_y(i) & y(i)\cdot f_y(i) \end{pmatrix},$$

where x,y and f_x,f_y are the respective components of the vectors $\mathbf{r}$ and $\mathbf{f}$. It is easy to show that due to the vanishing net force the components of $\overrightarrow{\overrightarrow{M}}$ are independent of the choice of the origin of the coordinate system. Moreover, the generalized first moment tensor is symmetric because the net torque vanishes. Thus it can be diagonalized. The sum of both eigenvalues λ_1, λ_2 has a simple interpretation. As the trace of a tensor is invariant under coordinate transformation $\lambda_1+\lambda_2=\Sigma_i \mathbf{r}(i)\mathbf{f}(i)$, i.e., the trace of the generalized first moment tensor corresponds to the sum of the contractile force components weighed by the distance of the adhesion sites from the center of the cell. This is most obvious if one chooses the center of the cell as origin of the coordinate system. In many instances, cells of similar sizes are compared (e.g., myocytes on substrates of different elasticity). In all other cases one can use the sum of all contracting force components. As contracting force we consider the projection of each force vector on the direction to the center of gravity of the cell. The eigenvectors of $\overrightarrow{\overrightarrow{M}}$ give the two major directions of the contracting force pattern. They are normal to each other. The dynamics of cell contractions can be conveniently characterized by the sum of the eigenvalues at each time step, e.g., Fig. 6(d).

For reasons of numerical stability we subtracted the averaged force of all adhesion sites (which is a small quantity and solely due to experimental noise) from each force contribution for the calculation of the generalized first moment. Moreover, we chose the center of the cell as origin of the

coordinate system. The generalized first moment tensor proved to be a very robust quantity. We deliberately omitted adhesion sites, assigned wrong locations or chose superfluous positions for force calculations, and found barely any change in the first moment tensor. Thus the generalized first moment tensor is a valuable tool even in situations where the contributions of single adhesion sites cannot be discerned clearly. Examples for first moment calculation are shown in Figs. 5(c) and 6(c) and give values in the range of 25 pNm for fibroblasts and 6 pNm for myocytes upon contraction. Thus our results are comparable to published data on fibroblasts (10 pNm) (Ref. 13) and human airway smooth muscle cells (3 pNm).[14]

IV. DISCUSSION

The main goal of this work was the development of a system for stable, reproducible, and high resolution cell force analysis. Such a system needed to be suitable for various cell types and capable to analyze cell forces applied on various time and length scales. As forces are applied by almost any cell at any time such a system could have a large impact for the understanding of cell function. This is most obvious for muscle cells whose main function is force generation or for connective tissue cells whose function is tissue stabilization. In addition, cell movement, an essential process, e.g., cells of the immune system, depends on force generation.

We chose cross-linked PDMS as substrate as it is transparent and tunable in its elasticity. In addition, cross-linked PDMS is biocompatible and its slight hydrophobicity allows easy surface coating with any extracellular protein by physisorption. Characterization of material properties can be performed in air without time limitations, as PDMS is free of water and other volatile substances. Thus mechanical properties of PDMS, such as viscoelasticity, Young's modulus, and Poisson's ratio, can be determined reliably. We found Poisson's ratio of 0.5 for any elasticity analyzed. Furthermore, viscoelastic behavior could be identified. The relaxing part of the modulus was between 10% and 35% of the elastic part. As most cell forces are applied on relativity long time scales, the dissipative part can be neglected in most instances. For fast applied cell forces as cell contractions, our calibration system allows in principle to incorporate the viscoelastic component into force calibrations. For our experiments elastic substrates from 1 MPa down to 16 kPa were created by using defined ratios between base and cross-linker. The results were highly reproducible with variations in Young's modulus of up to 10%. Preliminary experiments indicate that even softer PDMS films can be produced. As those elasticities correspond to the stiffness range of many organs and tissues (e.g., skeletal muscles), elastic substrates from PDMS can be used to study elasticity dependent phenomena of living cells such as differentiation.[5] Although other polymers such as polyacrylamide hydrogels allow the fabrication of even softer substrates below 1 kPa, PDMS is well suited for many cell types and scientific questions, with the additional benefit of long shelf lives of the substrates. We found no change in elasticity for time periods up to two months which was the longest period tested so far.

Video microscopy and subsequent image processing allowed the analysis of cell forces at places of focal adhesions. These adhesion sites were identified mainly by RICM. This technique had the advantage of visualizing both the micropattern and therefore the deformation field as well as the focal adhesions. Adhesion sites were characterized as dark spots and compared in place for cells simultaneously expressing GFP-vinculin. As identical areas were defined by both methods we preferred RICM analyses. This technique allows the analysis of any given cell independent of transfection efficiency and putative overexpression artifacts.

Our system is defined by a regular micropattern on top of an essentially flat PDMS substrate. As this micropattern consists just of pits, deep enough to yield good contrast in RICM but shallow enough not to get recognized by the cell, the elastic properties of the substrate material remain unaffected. The more widespread alternative, embedding rigid fluorescent microparticles into the materials, results in superbly contrasted images but is always accompanied by local and pronounced variation of material stiffness. As we do not know up to now which length scale is decisive for cellular mechanosensing, the influence of such microheterogeneity on the results is difficult to assess. Flat substrates additionally allow the characterization of cell forces over a long time period or during differentiation processes as the surface topography remains unaffected even upon ECM secretion of adhered cells. The latter effect often causes problems in micropillar systems as ECM proteins often act as glue pasting the pillars together (*bunching*).

Producing regular microstructures is a time consuming task relying upon the elaborate and expensive semiconductor device fabrication technology. However, the regularity of the resulting micropatterns is the strongest advantage of our approach. For deformation fields limited to one field of view of the microscope image processing enable us to localize the origin and the lattice vectors of the regular grid of the microstructure within one micrograph. This regular lattice is the reference frame defining the positions of the microstructures in the absence of mechanical forces. Such a reference frame is mandatory for determining deformation fields. If irregular microstructures are used, a corresponding reference frame can be obtained either by waiting for a locomoting cell to leave the field of view or by scratching away a stationary cell. Because the microstructured surface must not be changed in any way, the latter procedure is error prone and time consuming. Thus, regular microstructures are extremely useful especially for the study of stationary, i.e., most cells. An additional benefit of lithographically produced regular micropatterns is the freedom to choose grid (e.g., square or trigonal) and lattice constant according to the experimental system. As the shallow micropattern has no effect on substrate response, the only drawback of low lattice constants are the larger runtime of image processing programs and reduced contrast in micrographs.

Cells of the same type vary in size and number of adhesion sites. Such variations become even more prominent if different cell types are analyzed. A comparison of cell forces on the level of focal adhesion is therefore not always evident. By generalized first moment analyses as performed here, the

sum of all contracting forces is relatively independent of the number of focal adhesions. In addition, cell size variations can be taken into account. These analyses therefore allow a direct comparison of cell forces within an identical cell population, between different cell types or over time for processes as differentiation or adaptation.

ACKNOWLEDGMENTS

The authors thank Nils Hersch and Simone Born for skilled work in cell culture and microscopy. They are grateful to Benjamin Geiger for the GFP-vinculin construct. One of the authors (U.S.S.) was supported by the Center for Modelling and Simulation in the Biosciences (BIOMS) at Heidelberg University as well as by the Emmy Noether Program of the German Research Foundation (DFG).

[1] B. Geiger, A. Bershadsky, R. Pankov, and K. M. Yamada, Nat. Rev. Mol. Cell Biol. **2**, 793 (2001).
[2] A. D. Bershadsky, N. Q. Balaban, and B. Geiger, Annu. Rev. Cell Dev. Biol. **19**, 677 (2003).
[3] V. Vogel and M. Sheetz, Nat. Rev. Mol. Cell Biol. **7**, 265 (2006).
[4] D. E. Discher, P. Janmey, and Y. L. Wang, Science **310**, 1139 (2005).
[5] J. M. Goffin, P. Pittet, G. Csucs, J. W. Lussi, J. J. Meister, and B. Hinz, J. Cell Biol. **172**, 259 (2006).
[6] A. K. Harris, P. Wild, and D. Stopak, Science **208**, 177 (1980).
[7] T. Oliver, M. Dembo, and K. Jacobson, Cell Motil. Cytoskeleton **31**, 225 (1995).
[8] M. Dembo and Y. Wang, Biophys. J. **76**, 2307 (1999).
[9] S. Munevar, Y. Wang, and M. Dembo, Biophys. J. **80**, 1744 (2001).
[10] N. Balaban *et al.*, Nat. Cell Biol. **3**, 466 (2001).
[11] L. D. Landau and E. M. Lifshitz, *Theory of Elasticity*, 3rd ed. (Butterworth-Heinemann, Oxford, UK, 1986).
[12] M. Dembo, T. Oliver, A. Ishihara, and K. Jacobson, Biophys. J. **70**, 2008 (1996).
[13] U. S. Schwarz, N. Q. Balaban, D. Riveline, A. Bershadsky, B. Geiger, and S. A. Safran, Biophys. J. **83**, 1380 (2002).
[14] J. P. Butler, I. M. Tolic-Norrelykke, B. Fabry, and J. J. Fredberg, Am. J. Physiol. **282**, C595 (2002).
[15] W. A. Marganski, M. Dembo, and Y. L. Wang, Methods Enzymol. **361**, 197 (2003).
[16] Y. Xia and G. M. Whitesides, Annu. Rev. Mater. Sci. **28**, 153 (1998).
[17] J. L. Tan, J. Tien, D. M. Pirone, D. S. Gray, K. Bhadriraju, and C. S. Chen, Proc. Natl. Acad. Sci. U.S.A. **100**, 1484 (2003).
[18] O. Du Roure, A. Saez, A. Buguin, R. H. Austin, P. Chavrier, P. Silberzan, and B. Ladoux, Proc. Natl. Acad. Sci. U.S.A. **102**, 2390 (2005).
[19] H. Levinson, *Principles of Lithography* (SPIE-The International Society for Optical Engineering, Bellingham, WA, 2001).
[20] E. Zamir, B. Z. Katz, S. Aota, K. M. Yamada, B. Geiger, and Z. J. Kam, J. Cell. Sci. **112**, 1655 (1999).
[21] B. Jähne, *Digital Image Processing* (Springer, Berlin, 2005).
[22] J. C. Russ, *The Image Processing Handbook*, 4th ed (CRC, Boca Raton, FL, 2002).
[23] M. Abercrombie and G. A. Dunn, Exp. Cell Res. **92**, 57 (1975).
[24] K. Imanaka-Yoshida, M. Enomoto-Iwamoto, T. Yoshida, and T. Sakakura, Cell Motil. Cytoskeleton **42**, 1 (1999).
[25] U. S. Schwarz, N. Q. Balaban, D. Riveline, L. Addadi, S. Bershadsky, S. Safran, and G. Geiger, Mater. Sci. Eng., C **23**, 387 (2003).